






Article

Far-Wake Meandering of a Wind Turbine Model with Imposed Motions: An Experimental S-PIV Analysis

Navid Belvasi ^{1,*}, Boris Conan ², Benyamin Schliffke ², Laurent Perret ², Cian Desmond ³, Jimmy Murphy ¹ and Sandrine Aubrun ²

¹ MaREI Centre, Environmental Research Institute, University College Cork, P43 C573 Cork, Ireland

² Nantes Université, Ecole Centrale Nantes, CNRS, LHEEA, UMR 6598, F-44000 Nantes, France

³ Gavin & Doherty Geosolutions Ltd., D14 X627 Dublin, Ireland

* Correspondence: nbelvasi@ucc.ie

Abstract: Intra-array wake meandering increases fatigue loading in downstream turbines and decreases farm total power output. In the case of floating offshore wind turbines (FOWTs), the motions of the floating substructure could have a non-neglectable contribution to wake meandering dynamics. This research experimentally analyses the influence of imposed motions on the far-wake meandering of a FOWT. The study considers a 1:500 scaled porous disc representation of the 2 MW FLOATGEN system (BW Ideol) located off the coast of Le Croisic, France. A representative marine neutral atmospheric boundary layer is generated in a wind tunnel whilst monochromic and multi-frequency content three degrees of freedom (surge, heave, pitch) motion is imposed on the model tower. The stereoscopic particle image velocimetry (S-PIV) is then utilised to measure velocity vectors at a cross-section located at 8.125 D downstream of the model. No significant effect on the far-wake recovery in the velocity, turbulence and turbulent kinetic energy distribution is observed. However, the frequency characteristics of the imposed motions were observed in the far-wake meandering spectral content and streamwise characteristics of far-wake, such as normalised available power. While the frequency spectrum of the vertical oscillations showed more sensitivity to the three degrees of freedom (3DoF) imposed motion in all frequency ranges, the lateral oscillation was sensitive for the reduced frequency above 0.15. The monochromic motions with a reduced frequency of less than 0.15 also did not influence the far-wake centre distribution in both lateral and vertical directions. Regardless of reduced frequency, imposed motions show a strong effect on average power, in which the harmonic signature can distinguish in far-wake memory. This study provides an investigation, which its result could be beneficial to developing and examining wake models for offshore wind turbines, with a particular focus on the influence of FOWTs motions.

Keywords: far wake meandering; floating offshore wind turbine; imposed motions; far wake power fluctuation; stereoscopic particle image velocimetry; wind-tunnel experiment



Citation: Belvasi, N.; Conan, B.; Schliffke, B.; Perret, L.; Desmond, C.; Murphy, J.; Aubrun, S. Far-Wake Meandering of a Wind Turbine Model with Imposed Motions: An Experimental S-PIV Analysis. *Energies* **2022**, *15*, 7757. <https://doi.org/10.3390/en15207757>

Academic Editor: Qingshan Yang

Received: 15 September 2022

Accepted: 18 October 2022

Published: 20 October 2022

Publisher's Note: MDPI stays neutral with regard to jurisdictional claims in published maps and institutional affiliations.



Copyright: © 2022 by the authors. Licensee MDPI, Basel, Switzerland. This article is an open access article distributed under the terms and conditions of the Creative Commons Attribution (CC BY) license (<https://creativecommons.org/licenses/by/4.0/>).

1. Introduction

It is estimated that by 2050 the total installed floating wind energy capacity will reach 250 GW [1]; however, the deployment of the technology at the array scale is in the pre-commercial stage, and further fundamental studies are required to better understand intra-array dynamics. A critical ongoing research field in wind farms and, more specifically, floating offshore wind farms is studying wind turbine (WT) wake interactions. An overview of the state-of-the-art of these analyses is provided in [2–6]; where research topics such as performance and power losses of wind turbines due to wind turbine wake interactions in model and prototype scale are reviewed and addressed. In a wind farm, while the upstream turbines extract the kinetic energy of the incoming wind in undisturbed—inflow conditions, the downstream turbines operate in waked conditions. The wakes of upstream turbines influence the performance and the loading of subsequent located downstream

within the array. Based on observations [7], intra-array wakes result in an average power loss in an order of 10–20% in the farms total power output. Research on wake-induced fatigue loading for wind turbines [8] indicates that this generated wake increases fatigue loading up to 15% for the downstream WTs.

Turbine wake tends to fluctuate within the atmospheric boundary layer (See Figure 1), a phenomenon known as wake meandering, which causes the turbine wake region to have a fluctuating movement in the lateral and vertical directions. As a large-scale low-frequency movement of the whole wake region, this far-wake instability forces the wake area to be swept inside and outside of the rotor plane of the downstream turbine; hence, it plays a critical role in the design and optimisation of wind farms. This phenomenon tends to cause extreme loading and fatigue load cases [9] for downstream turbines. Among ongoing research, rich studies on wake meandering, such as the dynamic wake meandering model [10] should also be mentioned, where a physically based theory for the wake meandering phenomena is developed, and a focus has been set on describing the physical process of this phenomenon. As discussed in the literature [11], this large-scale movement of the entire wake area could be forced by large-scale eddies structures present in the atmospheric boundary layer that advected downwind. Another possibility of this behaviour is the aerodynamic instability because of the vortex shedding behind the turbine rotor itself since it could act as a bluff body. A combination of both causes could also be the reason for the wake meandering phenomenon. While the first cause is widely measured in real-world demos, the second is more seen in laboratory measurements [11].

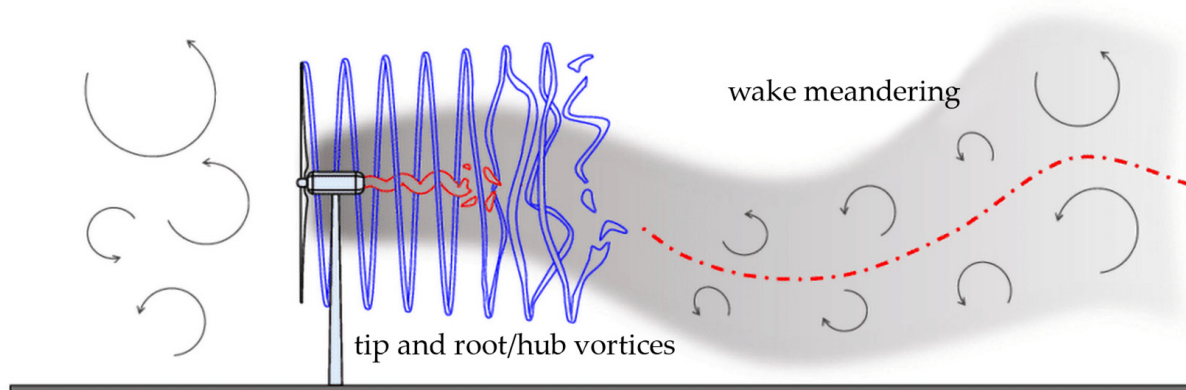


Figure 1. Schematic of wake meandering [12].

The wake meandering effects are even more critical in offshore conditions. Due to reduced ambient turbulence and so less turbulent diffusion of the wake, the recovery of turbine wakes can be significantly delayed, for instance, see [13]. Moreover, the atmospheric turbulent eddies are larger in offshore fields; therefore, more meandering is expected. Importantly, FOWTs substructure motions have the same order of magnitude compared to the energetic turbulence scale of the atmosphere and the characteristics of the wake [14]. As a result, substructure motions due to the environmental loading could potentially influence the wake meandering process. Given the increasing complexity of wakes caused by offshore platform motion, these effects make the area poorly understood in the case of floating wind.

The degrees of freedom (DoF) of FOWTs make their wake structure more complex to study. Research on a model wind turbine with imposed pitch and roll was carried out by [15]. In this experiment, employing particle image velocimetry and hotwire anemometry, the impact of a range of roll and pitch oscillations (with the reduced frequency range of 0.008–0.017 and the amplitude of 5° – 20°) on the wake and output power of a floating wind turbine was studied. This study revealed that the imposed motions significantly alter the wake at the turbine symmetry plan. Research [16] was carried out on the effect of pitching on the characteristics of the turbulent intermittency in the wake of a wind turbine. This research considered two inflow conditions with 1.8% and 15% turbulence intensity. It

shows that the flow behind a pitching wind turbine is more intermittent when compared to a fixed wind turbine. Another study [17] investigates the effect of imposed surge motion on the wake characteristics of a wind turbine model. A porous disc at a scale of 1:500 was used, having two analysis approaches: fixed frequency with varied amplitude; and fixed amplitude with varied frequency. In the spectral analysis, the frequency of the surge motion was observed in the wake spectral content at longitudinal distance equal to 4.6 times rotor diameter ($x > 4.6 D$).

While reviewing the literature shows a non-neglectable influence of the FOWTs motions on the downwind flow condition, an open research question is to investigate if these motions could also alter the development of the wake meandering process. The main aim of this research paper is to determine the influence of the FOWT substructure motion in the far-wake ($x > 8.125 D$) meandering process and investigate if this influence can be neglectable or should be considered for further wake model development. Most recently, research in this area has focused on the surge motion signature in the wake meandering of FOWTs [14]. The current study advances the state-of-the-art by extending to other motion DoFs, considering the monochromatic motions of pitch, as well as 3DoF motion (surge, pitch, heave) with multi-frequency content time series. A wind turbine model made of porous disc representing the full-scale 2 MW FOWT FLOATGEN (BW-Ideol) demonstration project [18] is used. The porous disc model with a reduced scale of 1:500 respects geometric and kinematic similarities with a real floating wind turbine prototype. The wakefield of this porous disc at the distance of 8.125 D in crossflow direction is interrogated using stereoscopic particle image velocimetry (S-PIV). The paper then provides results based on high fidelity velocity vectors to analyse the instantaneous wake centres statistics in crossflow direction, as well as normalised available power in far-wake in streamwise direction, both downstream of the turbine model.

The remained of this paper is divided into three main sections. In Section 2, the experimental configuration, methodology, and data-processing approach are defined. In Section 3, the results of the measurements are presented and discussed, in which data quality metric on the immediate measurements data is applied. Then, the wake meandering process is reviewed in four main subsections, including recovery of the far-wake, statistics of the meandering process in the time and frequency domain, as well as normalised available power in the far-wake. In each subsection, a discussion on results is made. Finally, in Section 4, conclusions are provided, and key findings are summarised.

2. Experimental Setups

2.1. Wind Tunnel and Flow Condition

The experimental campaign is conducted in the open-circuit atmospheric wind tunnel at LHEEA (Research Laboratory in Hydrodynamics, Energetics and Atmospheric Environment) test facilities in Ecole Centrale Nantes, France. The wind tunnel is 26 m long with a cross-section of 2 m \times 2 m. The centrifugal fan of the wind tunnel is powered up by a 45 kW motor, allowing it to reach the maximum wind speed of 10 m/s with the freestream turbulence intensity T_i around 1.2%. This facility has been used in the past for atmospheric boundary layer (ABL) studies in the scale-ratio range of 1:200 [19] and 1:500 [14,17,20]. In order to generate the ABL condition, the wind tunnel is equipped with a set of turbulence generators, a fence at the entrance of the test section, as well as perforated metal plates on the floor. Over an 18 m fetch length, these elements produce the boundary layer (BL) with the characteristic of a marine boundary layer at a geometric reduction scale of 1:500. The current ABL model is based on environmental meteorology standards, fully described in [17,21], where the identical setup for ABL was used. This model represents the flow over the sea site with a power-law exponent of $\alpha = 0.1$, full-scale roughness length of $z_0 = 5.5 \times 10^{-6}$ m, and the full-scale integral length scale of $L_u^x = 200$ m, above a threshold of two times of the rotor diameter in full scale (160 m) [17]. These characteristics fall under the category of slightly rough terrain, based on the Cat. I VDI Guideline 3783 [22]. With

a reference wind speed of 2.85 m/s at hub height, the neutral incoming boundary layer has a turbulent intensity of 8% at hub height.

2.2. Model Description

The studied model is based on the FLOATGEN project [18], a 2 MW floating wind turbine with an 80 m rotor diameter and 60 m hub height. This real-scale prototype, with a barge-type substructure, was designed by BW Ideol and installed at the SEM-REV test site [23]. This demo project has been operational since 2018. In the current experimental study, the model wind turbine is represented at a scale of 1:500 with a porous disc, the fundamentals of which are discussed in [24]. The characteristics of the disc model are identical to [17]. With a metallic mesh, this porous disc is designed to produce the same far-wake as a three-bladed wind turbine. Considering the geometrical scaling factor of 1:500, the equivalent diameter for the porous disc is 160 mm, giving a blockage ratio of 0.5% in the test section. The disc comprises wires with a diameter of 1 mm and a thread spacing of 3.2 mm, resulting in a solidity ratio equal to 55%. This leads to the thrust coefficient of $C_T = 0.62$, the power coefficient $C_P = 0.25$, as well as an axial induction factor $a = 0.21$. The turbine tower is also modelled, using a rod with a diameter of $0.05 D$ (where D is turbine diameter), with a hub height equal to 120 mm. The model is shown in Figure 2.

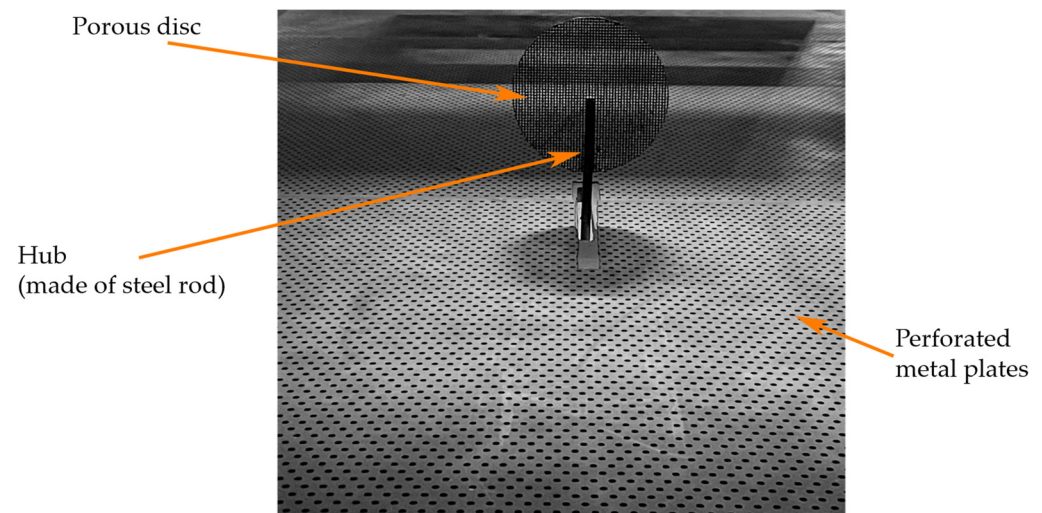


Figure 2. Porous disc model of the studied wind turbine.

The time-series of the substructure motion is imposed on the porous disc using a 3DoF motion system. These motions include surge, pitch, and heave oscillation. The imposed motions are presented in Table 1, which are imposed at the centre of gravity for the substructure located at the seawater level. In this table, motions type, amplitude, normalisation of amplitude based on the rotor diameter, frequency, as well as equivalent reduced frequency are presented. The reduced frequency is derived based on Equation (1).

$$f_{\text{red}} = \frac{f \times D}{U_{\text{ref}}} \quad (1)$$

where f is the frequency in Hz, D is porous disc diameter, and U_{ref} is the streamwise velocity at hub height without the presence of the wind turbine model, equal to $U_{\text{hub}} = 2.85$ m/s.

The order of magnitude of the imposed motions is selected based on numerical simulations provided by BW Ideol [18] and based on the sea condition at the test site location, which includes the significant wave height of $H_s = 4.25$ m, and peak period of $T_p = 11.25$ s. Due to the 1:500 scale ratio, the velocity and time scale factors are 2.5 and 200, respectively. The wind tunnel's power forces the current study to introduce velocity scaling, as reproducing the 8 m/s wind speed at hub height measured near SEM-REV was

not possible in the wind tunnel in practice. The velocity scaling also contributes to reducing the time scaling, which helps reduce the frequencies of the scaled-down motions.

Table 1. Test matrix for the imposed motions on the porous disc model.

Test Case	Model			Dimensionless Values	
	Motion Type	Amplitude	Frequency (Hz)	Normalised Amplitude **	Reduced Frequency
1	Fixed model	-	-	-	-
2	Pitch I *	8°	5	8°	0.28
3	Pitch II *	8°	2.5	8°	0.14
4	3DoF (Surge, heave, Pitch)	Time series		Time series	
5	Surge I	20 mm	2	0.125	0.11

* The mean pitch remained at 0°, i.e., no pitch offset. ** Translational amplitudes: normalised on rotor diameter; rotational amplitudes: no normalisation.

2.3. S-PIV Measurements and Data Analysing

The stereoscopic particle image velocimetry (2D3C) method [25] was used to measure the velocity components downstream of the porous disc. The fluid flow was seeded with a fine mist of olive oil droplets with a diameter of 1 μm . These droplets are sprayed at the beginning of the wind tunnel by a LaVision seeding system. These seeds are then illuminated in the area of interest using an Nd-YAG double cavity laser with 200 mJ energy per pulse. The laser is located at the top of the test section ceiling. The emitting pulses are 532 nm wavelengths with a time delay of 350 μs between pulses, and the emission rate is 14.1 Hz. The emitted light sheet was oriented to the cross-section of the test section and centred at a distance of 8.125 D downstream of the porous disc model. The cartesian coordinate system is used for the measurement in the wind tunnel, in which x , y , and z axis corresponds to the streamwise, lateral, and vertical directions, respectively. The light sheet illuminates the measurement area with the size of 0.2 m \times 0.4 m, vertical and perpendicular to the flow main directions (see Figure 3). To remove the background effect, i.e., the tunnel reflection due to laser emission, the test section and model is painted in matt black. The image acquisition system consists of a pair of sCMOS 5.5 Mpx HighSense Zyla cameras with 60 mm Nikon objectives lens. These cameras were located at the side windows of the tunnel, as shown in Figure 3. The whole system is synchronised to acquire pairs of images at the 14.1 Hz sampling rate, resulting in the Nyquist frequency of 7.05 Hz for frequency domain analysis, which is equal to the reduced frequency of 0.40. Due to the 14.1 Hz sampling frequency, the S-PIV device used here is not time-resolved. In order to estimate representative statistics [26], 14,000 image pairs per test case were recorded. The mean value of 14,000 images is subtracted from them to remove the remaining background effect present in all images. Data acquisition, synchronisation, and velocity vector processing are conducted with DANTEC DynamicStudio 6.1. A multi-pass adaptive correlation algorithm along with Gaussian peak fitting was used to calculate the velocity vectors. This algorithm is applied with an initial window size of 128 px \times 128 px; then, two refinement steps are applied to finally reach 32 px \times 32 px interrogation windows with 50% overlap. The resultant two-component velocity maps of each camera are then combined to form instantaneous three-component velocity vectors. Quantifying the associated error to the S-PIV technique is out of the scope of this study; however, a review of the source of errors and uncertainties for PIV measurements can be found in [27]. The post-processing of velocity vectors for the wake centre tracking purpose is carried out with a developed Python code based on the maximum convolution between the field of instantaneous available power and a Gaussian masking function. The method is comprehensively explained in [14].

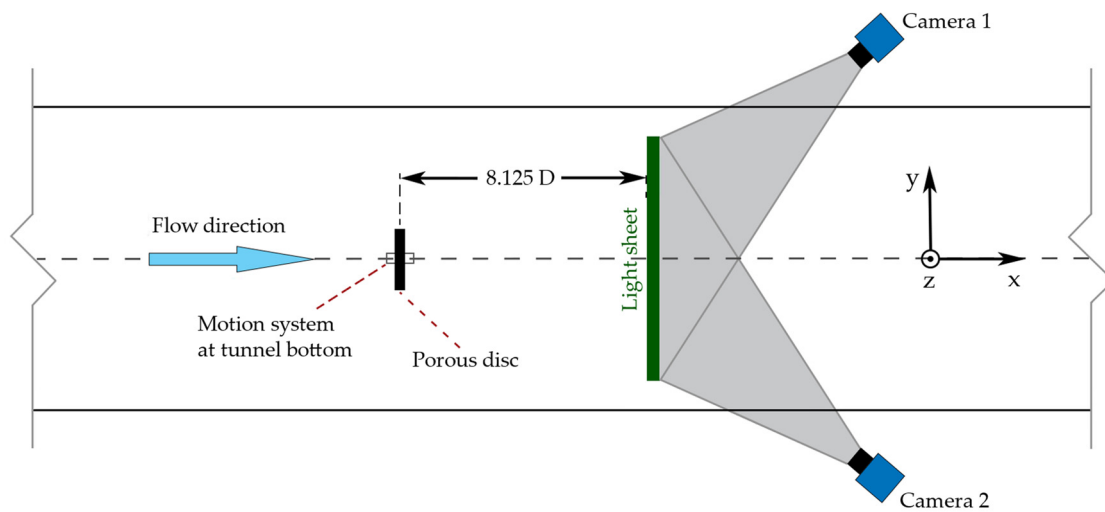


Figure 3. Arrangement of the turbine model and S-PIV measurement system.

3. Results

The effect of floating turbine motion on wake meandering is investigated in this section. In Section 3.1, a quality metric is applied to the detected wake centres to calculate the statistical uncertainty in the wake centre data. Then, the velocity and turbulence distribution for different test cases is investigated in Section 3.2. Next, statistics of the wake meandering are studied. Data are then transformed to the frequency domain using Welch (periodogram) method for frequency domain analysis. Finally, the effect of imposed motion on the power in the far-wake of the turbine model is analysed. In all comparisons, the fixed test case (case no. 1 in Table 1) is considered the reference case; other test cases are then reviewed with the reference case. This approach allows us to investigate motions influence on the wake characteristics, once separately and then all together.

3.1. Data Quality Metrics

In order to reach a statistical convergence for the velocity field and its fluctuation, i.e., standard deviation, the number of $n = 14,000$ image pairs is taken by cameras for each test case. Considering this number of images and the sampling rate of 14.1 Hz for S-PIV synchronised acquisition, it results in the length of $t = 992.8$ s for each time series. According to [26], an initial relative uncertainty estimation can be achieved by assuming a Gaussian distribution for velocity fluctuations. Therefore, the convergence uncertainty of the mean velocity and standard deviation of the velocity is estimated through (2) and (3), respectively.

$$\epsilon_{\langle u \rangle} = \frac{Z \cdot I_u}{\sqrt{N_b}} \quad (2)$$

$$\epsilon_{\sigma} = \frac{Z}{\sqrt{2N_b}} \quad (3)$$

where I_u is turbulent intensity in the streamwise direction, which for the current study it is equal to 8%. The Z is parameter of the confidence intervals. According to [26], the parameter Z is equal to 1.96 for the confidence interval of 95%. Moreover, N_b is the number of independent samples, which is the ratio between time-series duration of 992.8 s to the integral time scale, i.e., the time scale of each motion. According to [28], the separation of two integral length scales between two samples is required to ensure independence of the samples, therefore, two times of integral length scale is considered to calculate N_b in the current study. Taking all together, the relative uncertainty at hub height, in the captured velocity field, and its standard deviation is in the range of 0.31 to 0.49% and 2.78 to 4.39%, respectively. In addition to the statistical error, a bias error (with a unit of m/s exists)

resulting from the S-PIV processing of DANTEC DynamicStudio 6.1, approximately equal to 0.1 pixels per local displacement.

3.2. Recovery of Far-Wake

The statistics of the far-wake velocity field, including the streamwise velocity profile and its standard deviation and turbulent kinetic energy, are shown in Figures 4 and 5. In the first figure, these values are measured at hub height and plotted against the lateral distance ($Y.D^{-1}$), in second figure they are measured at $y = 0$ and plotted versus heights of $(z - z_{\text{hub}}).D^{-1}$. These velocity profiles are calculated based on the resultant mean velocity from the S-PIV images, normalised by the freestream velocity. The investigation on the current incident ABL is provided in [17], where the incident non distributed flow as well as flow with the presence of the porous disk is provided. The freestream velocity is $U_{\text{Ref}} = 2.85$ m/s, which is the streamwise velocity at hub height without the presence of turbine model. Noted, that the non-symmetric shape of the velocity profile in the vertical direction (see Figure 5A) is because that profile is a superposition of the velocity profile of porous disc wake, as well as the incoming ABL. This non-symmetric shape is in line with the wind tunnel studies conducted in the literature, for instance [29].

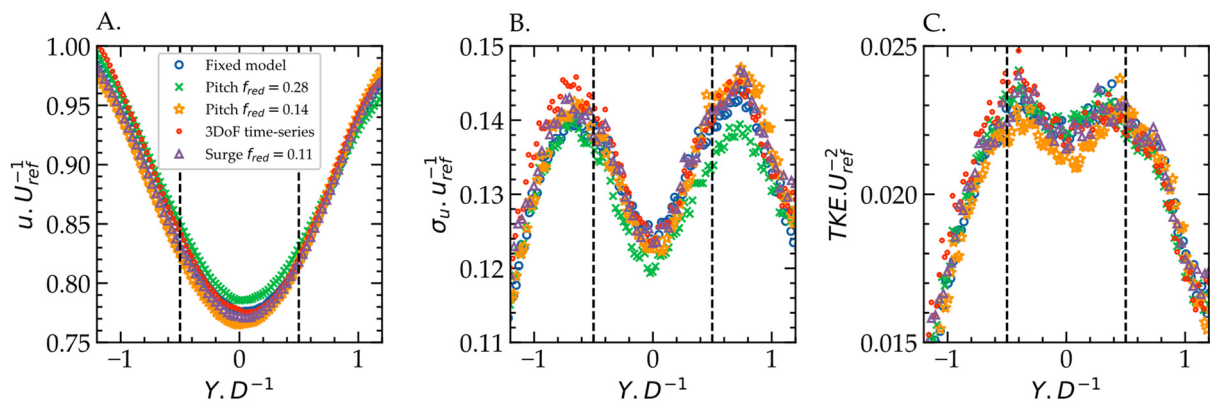


Figure 4. Statistics of the far-wake velocity field at hub height ($Z = 0$) versus the lateral distance; (A) Streamwise velocity; (B) Standard deviation of streamwise velocity; (C) Turbulence kinetic energy (TKE).

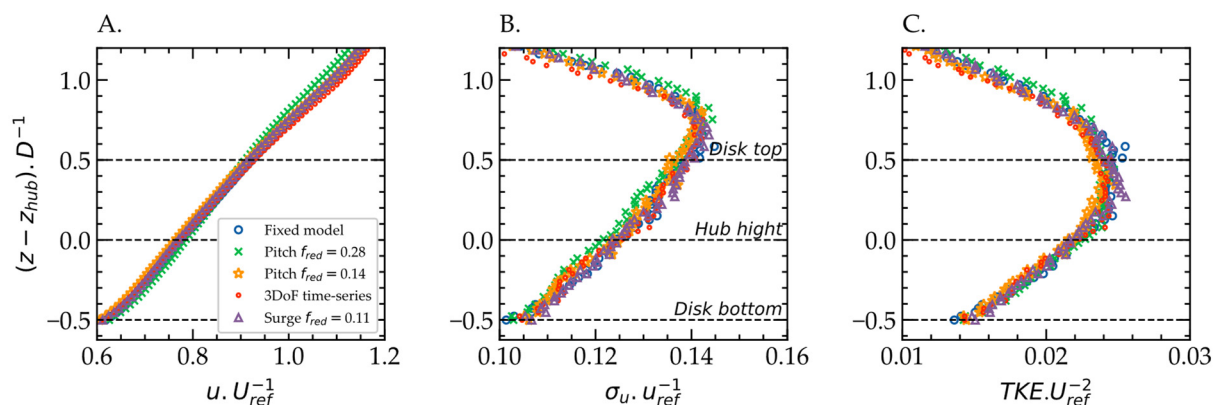


Figure 5. Statistics of the far-wake velocity field at turbine centreline ($Y = 0$) versus the height; (A) Streamwise velocity; (B) Standard deviation of streamwise velocity; (C) Turbulence kinetic energy (TKE).

The statistics of the velocity field for different test cases follow the trend and values of the fixed case velocity distributions in lateral and vertical directions. The same pattern can

be observed for the Turbulence kinetic energy (TKE) in both Figures 4 and 5. The TKE is defined based on (4).

$$\text{TKE} = \frac{1}{2} (\sigma_u^2 + \sigma_v^2 + \sigma_w^2) \quad (4)$$

where σ_u , σ_v , and σ_w are standard deviations of velocity in streamwise, lateral, and vertical directions, respectively.

It can be observed in Figures 4 and 5 that the imposed motions, including the multi-frequency contest motion (namely 3DoF time-series in the figures), have a neglectable effect on the mean wake recovery in the far-wake (8.125 D). Taken all together, these graphs suggest that at 8.125 D downstream of the turbine for the DoFs imposed and in the range of frequency/amplitude tested, far-wake velocity and turbulence distribution have no sensitivity to imposed motions. Prior wind tunnel studies, for instance [17], also discussed that monochromatic motions have no influence on the wake recovery for distance over 4.6 D from the disc model. Therefore, the findings of the current study are suggesting that multi-frequency content motions also have no influence on the far-wake (8.125 D) recovery.

These findings are contrary to recent research studies [30,31], which have suggested that surge and pitch motion of the floating platform could affect the wake recovery of the turbine rotor. The inconsistency between the result of wake recovery of the current research paper and [30,31] could be due to two reasons. Firstly, in that research a larger 15 MW wind turbine (WT) is used, while here a 2 MW wind turbine model is studied. Secondly, the flow configuration of [30,31] are significantly different to the current research study. Here, a marine neutral ABL is induced to the model, while in [30] a laminar inflow condition, and in [31] the Mann turbulence grid box is utilized. In that case, the before-mentioned research mainly focuses on WT characteristics and the output quantities (such as power, thrust, tower motion, etc.) of a second WT downstream a moving WT. In contrast, the current research mainly focuses on wake properties.

3.3. Far-Wake Meandering Statistics

The statistics of the wake meandering for different test cases are investigated in this section. The 95% confidence interval of the wake centres variance is plotted in Figure 6A for each test case. Subplot A depicts the position of the mean wake centre compared to centre of the porous disk. The mean wake centres are slightly shifted compared to the hub and vary with testcases. There is no apparent reason for this random noise. The problem could be raised from a non-symmetrical fluid flow source in the test section. However, it does not affect the analysis of the wake meandering, as current research focuses on the signature of the motion frequency in the wake meandering frequency spectrum.

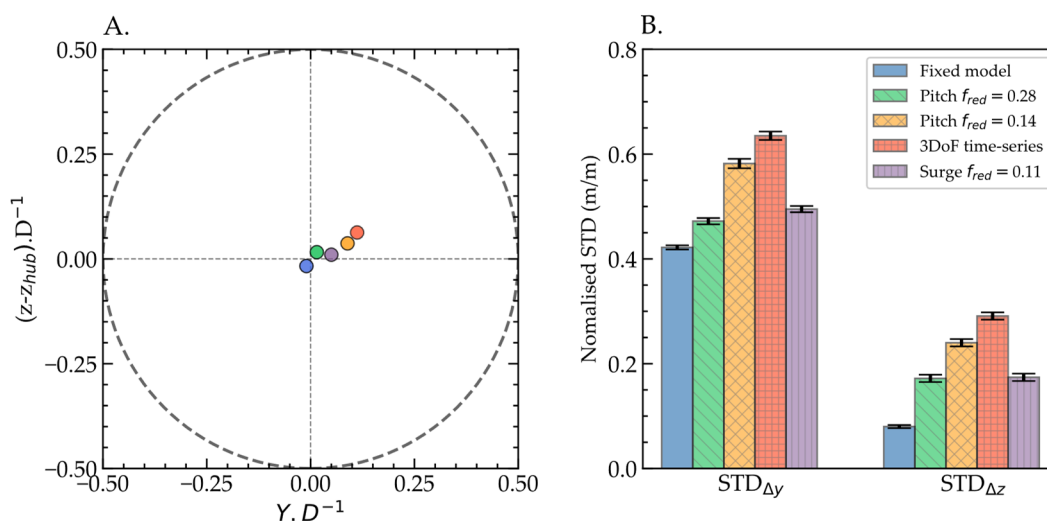


Figure 6. Evolution of the mean wake centres for different test cases at 8.125 D, in lateral and vertical directions: (A) Wake centres locations; (B) Standard deviations and its 95% confidence interval.

The standard deviation in two directions is represented in Figure 6B, and a 95% confidence interval is indicated on each bar and is normalized on the rotor diameter of the model wind turbine. Based on Figure 6B, it can be seen that difference between the standard deviations is significant, along with no overlap between ranges of confidence intervals. Therefore, one can conclude that estimated values are statistically distinguishable from each other.

In order to analyse the effect of the imposed motion on the wake centres, a special focus has been set on comparing the distribution of instantaneous wake centres with respect to the mean wake centre. So wake centres are revised based on Equation (5).

$$\begin{aligned}\Delta y &= y_c - \bar{y}_c \\ \Delta z &= z_c - \bar{z}_c\end{aligned}\quad (5)$$

where the (y_c, z_c) are instantaneous, and (\bar{y}_c, \bar{z}_c) are mean wake centres.

The detected wake centres are plotted as a 2D histogram in Figure 7; a dashed circle also shows the porous disc area. These wake centres are detected with a sampling rate of 14.1 Hz, resulting in 14,000 points for each test case. The 2D histogram is used to cluster the detected wake centres in an area of Y in the range $[-1.4, 1.4]D$ and Z in the range $[-0.6, 1.2]D$. The colour bar shows the density of the detected centres in each point location; accordingly, the clustered locations where more wake centre points are detected are plotted in dark red.

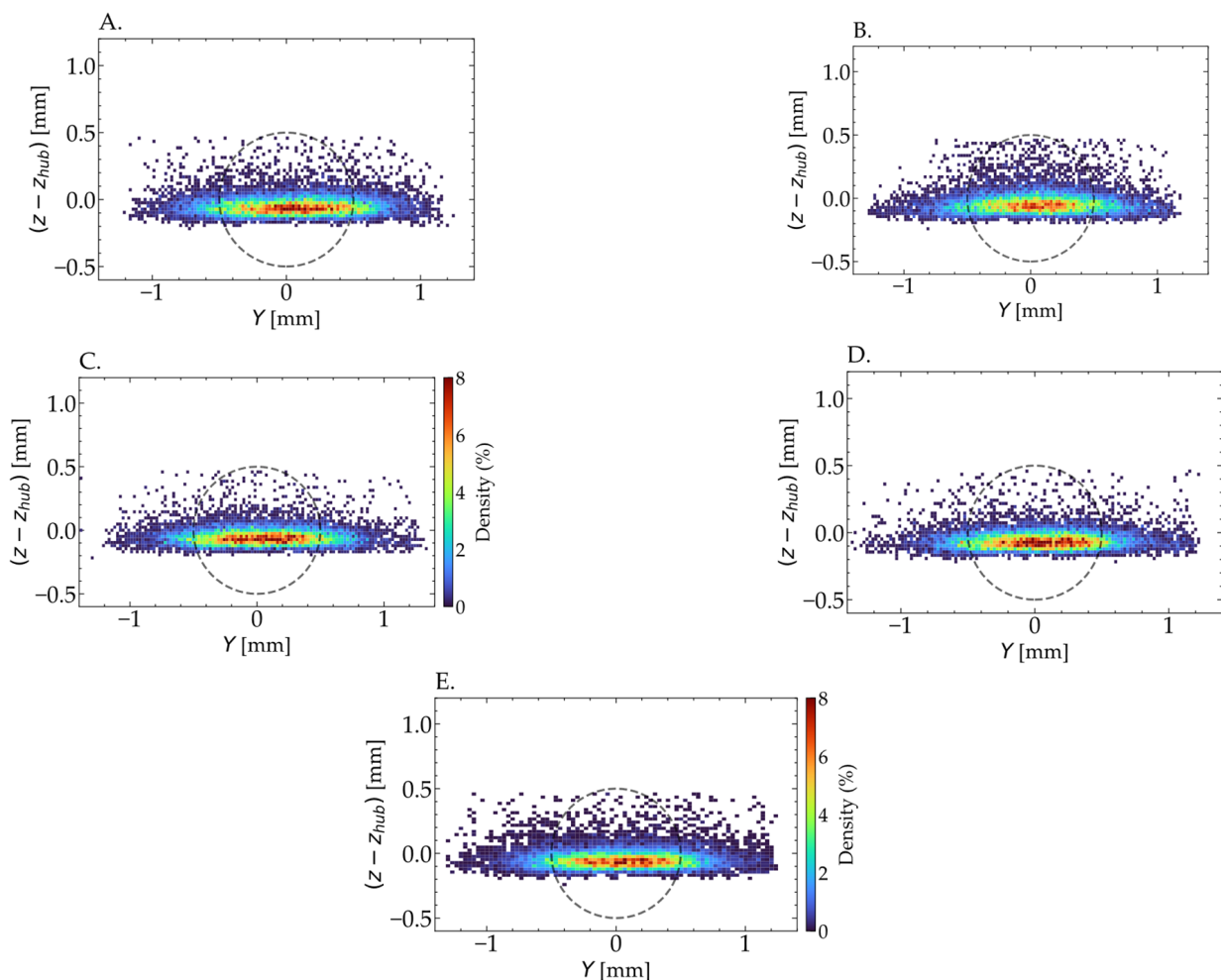


Figure 7. 2D histogram of wake centres for different test cases: (A) Fixed model; (B) Pitch $f_{red} = 0.28$; (C) Pitch $f_{red} = 0.14$; (D) 3DoF realistic time history; (E) Surge $f_{red} = 0.11$.

As can be observed in this figure, wake centres are more oscillating in the lateral direction than in the vertical direction. This behaviour complies with prototype observation [32] for fixed bottom turbines. Here, for the current study, it can be inferred that imposed motions of the substructure, including 3DoF multi-frequency content time series, do not alter this behaviour. Moreover, the wake centres are widely spread out of the rotor area in both lateral and vertical directions; this is mainly because the measurements plane is located at the far-wake (8.125 D), allowing the wake meandering to spread. This is well aligned with the model test observation in the literature, see [14,20,21,33].

No further pattern due to imposed motion can be observed in these 2D histograms; therefore, in Figure 8, these contours are broken into 1D histograms for better inspection. The probability density function (PDF) of the wake centres in the lateral and vertical directions is calculated and plotted in this figure. It is shown in Figure 8 that the wake centres distribution has a Gaussian shape in the lateral direction, while it has a narrow distribution with a skew-normal shape in the vertical direction. This discrepancy is because that vertical velocity fluctuations are damped due to the physical ground effect in the wind tunnel (as a wall boundary condition); hence no wake centres are detected below the $-0.25 D$. A similar condition is reported in [14], where the physical ground effects cause the same damping on wake centre locations. The ground effect caused the 1D histogram of wake centre vertical locations to be skewed toward positive values and highly tailed on the right side of the 1D histogram (i.e., higher altitudes).

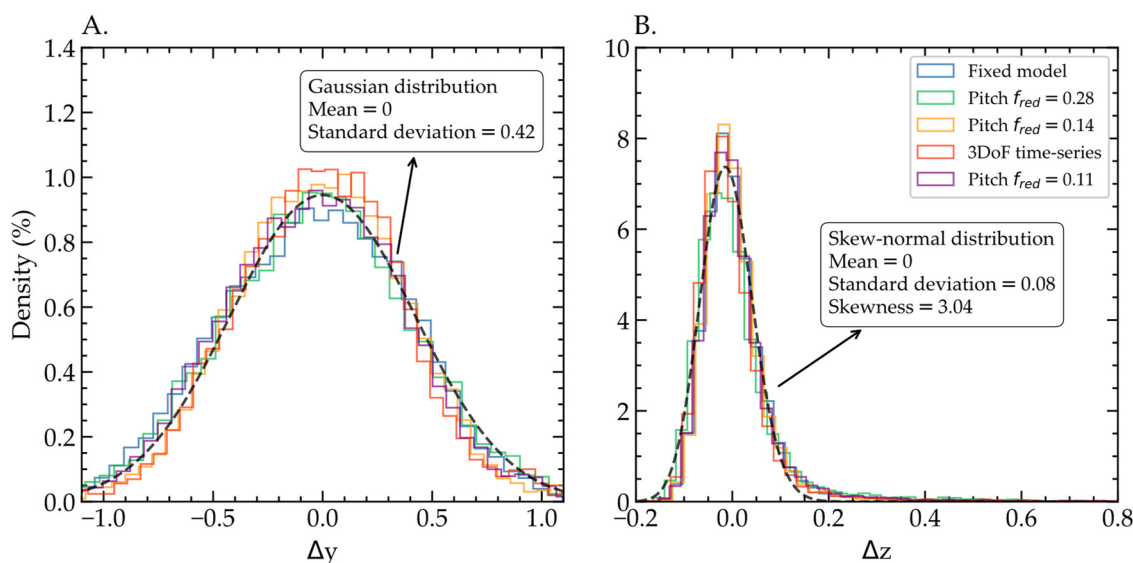


Figure 8. Probability density function (PDF) of wake centres lateral ((A) Δy) and vertical ((B) Δz) locations at $x = 8.125 D$.

The statistics of the wake centre time-series for different test cases are presented in Table 2, in which the standard deviation, skewness, as well as kurtosis are presented. Comparing the lateral and vertical time-series of wake centre oscillations, the higher values in standard deviations of lateral oscillations show that the instantaneous wake centres are more spread in the lateral direction for all test cases, as discussed earlier in this subsection. Meanwhile, the lower value for the skewness shows that the distribution of the wake centres in the lateral direction is symmetric in general compared to the vertical direction. Moreover, the kurtosis value shows that the distribution tail is heavier in the vertical direction rather than the horizontal. In reviewing the wake centre time history statistics, no pattern can be observed as an impact of the imposed surge, pitch, or multi-frequency 3D motions, as they all follow the random distribution shown in Figure 8. These investigations suggest that imposed motions on the substructure, including pitch, as well as multi-frequency content time series, have no visible effect on the wake centre distribution of the far-wake meandering process in the condition tested.

Table 2. Statistics of wake centre time histories.

Row	Test Case	Standard Deviation		Skewness		Kurtosis	
		Δy	Δz	Δy	Δz	Δy	Δz
1	Fixed model	0.422	0.080	−0.094	3.035	−0.396	17.521
2	Pitch I (Amp: 8°; f_{red} : 0.28)	0.472	0.172	0.326	4.331	0.572	22.585
3	Pitch II (Amp: 8°; f_{red} : 0.14)	0.582	0.240	0.737	3.313	1.000	10.934
4	3DoF realistic time-series (Surge, Heave, Pitch)	0.635	0.291	0.314	2.613	0.552	6.094
5	Surge (Amp: 20 mm; f_{red} : 0.11)	0.495	0.174	0.442	4.468	0.765	23.235

3.4. Spectral Analysis of Far-Wake Centres

The wake centre data are then processed into the frequency domain for further investigations. The frequency spectrum of wake centres time histories is calculated with the Welch method. The Welch method with the segment length of 128 samples and the overlapping ratio of 50% is employed. Moreover, as mentioned in Section 3.1, the duration of each time-series is $t = 992.8$ s. In Figure 9, the power spectral density (PSD) of y_c and z_c are shown for different imposed monochromatic motions. In each subplot, the reduced frequency of imposed motions is shown with a red dashed line. Note that due to the sampling rate of 14.1 of the S-PIV measurement, the Nyquist (or folding) frequency is equal to 7.05 Hz (equal to a reduced frequency of 0.4) for all frequency spectra. Closer inspection of the figure shows the influence of the motion frequency only for case B. Pitch $f_{\text{red}} = 0.28$. So that a peak is observable in the z_c -PSD of this test case in the reduced frequency of 0.28. No peak for other monochromatic motions can be observed in the subplots of Figure 9. This result accords with earlier wind tunnel experiments [17], which showed that the frequency of motion is observable in far-wake ($x > 4.6 D$) velocity spectra, only when the reduced frequency is $f_{\text{red}} > 0.15$. Similarly, studying the effect of imposed surge motions on the near and far-wake meandering [14] has shown no influence of the motions on the y_c and z_c PSD of the far-wake meandering, when the motion frequency was under this limit. Taken these all together, it can suggest that regardless of the induced monochromatic motion, the frequency of the substructure motion could affect the wake meandering centres fluctuation, only when the motion reduced frequency is over the limit of $f_{\text{red}} > 0.15$.

As the 3DoF case is based on the 3D multi-frequency motion time series, it contains a wide range of motion frequencies. To better review this spectrum with the reference test case, both are presented in Figure 10. As shown in the figure, compared to the fixed model, the model with imposed 3D motion has a different power spectral density for its lateral as well as vertical wake centres PSD. While the spectral content of the lateral position follows the fixed test case up to a reduced frequency of 0.15, the vertical position has a higher spectral content in all the frequency ranges, resulting in having more energy across all frequency ranges. This could interpret that in a realistic situation with the multi-content frequency of the FOWT substructure motions, these motions have a more significant influence on the vertical wake oscillation rather than the lateral oscillation in the wake meandering process.

To review the spread (variability) of the PSD of instantaneous wake centres, the box plot of PSD values of y_c and z_c is shown in Figures 11 and 12, respectively. The detected wake centres are separated into four equal parts, each presenting 25% of the data belonging to the power spectrum density of each test case. The fixed test case is plotted as the reference on the left side of the figures. As shown, for the cases with motions, the range of the detected wake centres is equal to the reference test case, with a positive skewness towards lower frequencies, showing a density of the data toward higher frequencies of motions. This combination of findings provides support for the conceptual premise that induced motions could not affect the wake meandering process when the induced motion frequency is under the $f_{\text{red}} = 0.15$ limit. As another observation, from Figure 12, it can be seen that for the case with 3DoF multi-content time series, the PSD content is over the

max value compared to the fixed references test case. This is not observed for the PSD of the lateral oscillations in Figure 11, supporting the conclusion that the effect of imposed motions with multi-frequency content is stronger for the vertical oscillation of the far-wake meandering.

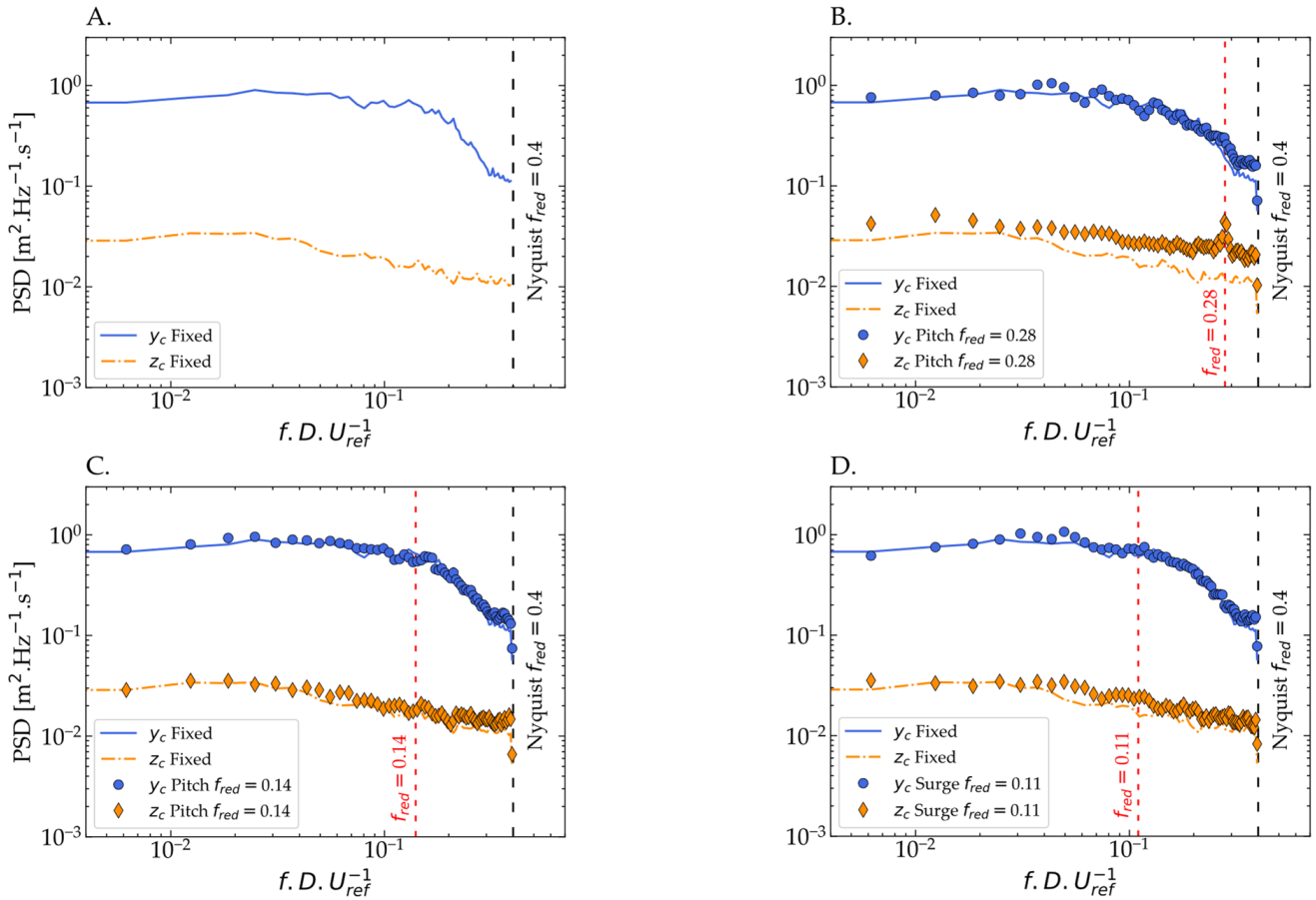


Figure 9. Spectral density spectrum of wake centres for different test cases. (A) Fixed model; (B) Pitch $f_{red} = 0.28$; (C) Pitch $f_{red} = 0.14$; (D) Surge $f_{red} = 0.11$.

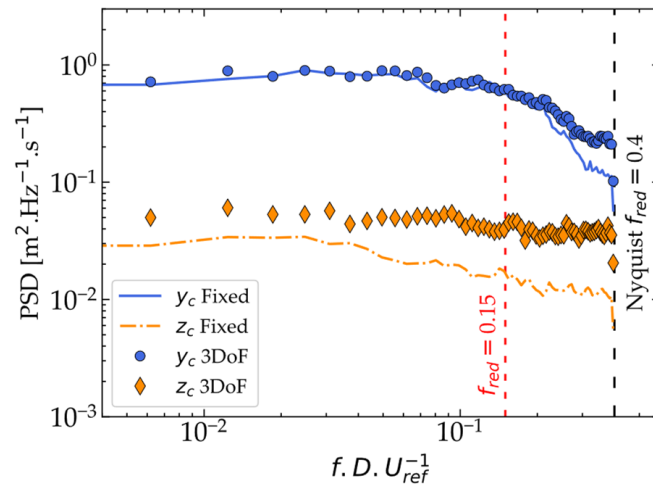


Figure 10. Comparison of the power spectral density (PSD) of lateral and vertical wake centre for the model with two cases of fixed and imposed 3D motion.

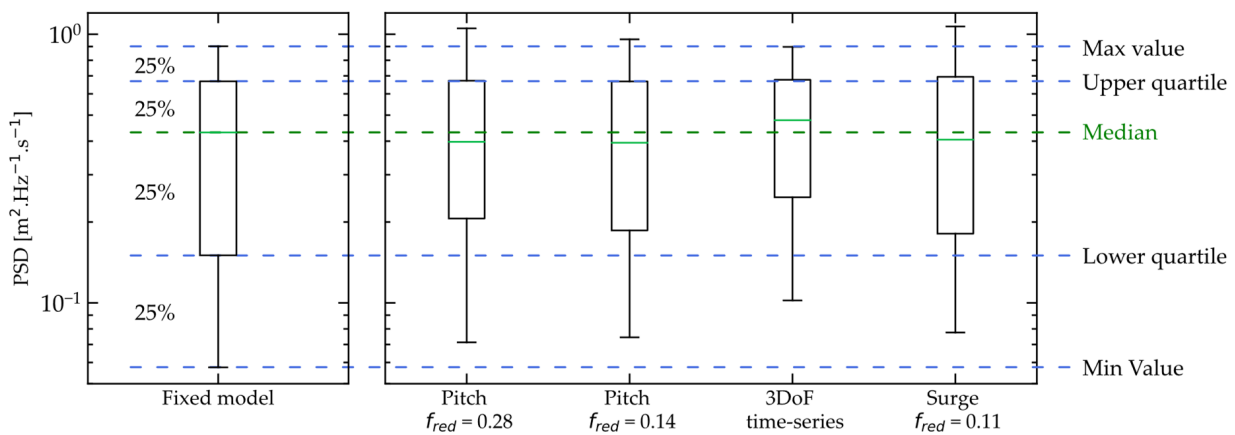


Figure 11. Box-and-Whisker plot of PSD values for y_c .

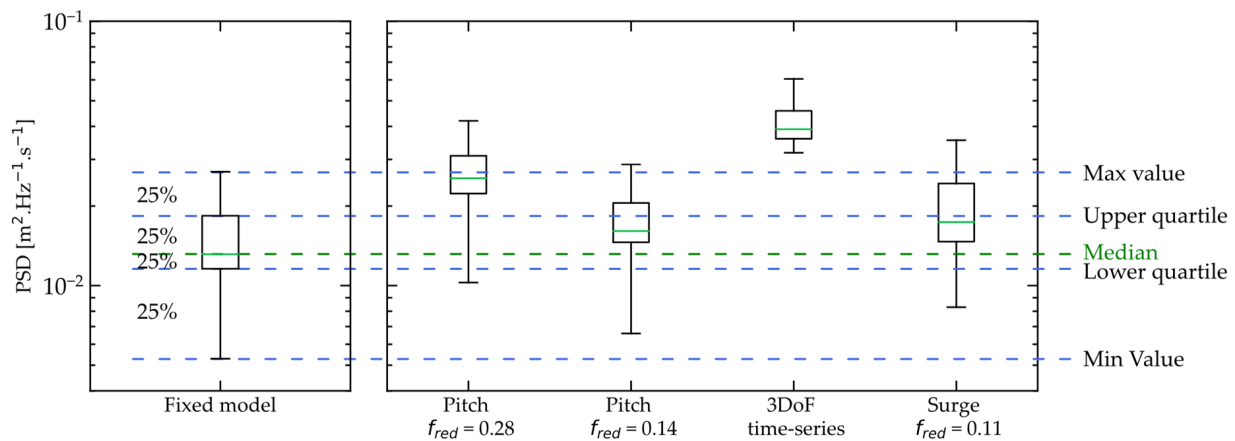


Figure 12. Box-and-Whisker plot of PSD values for z_c .

3.5. Normalised Available Wind Power

The present study was conducted to determine the effect of imposed motions on the far-wake meandering process in the lateral and vertical oscillation of the far-wake centres. The influence of imposed motions on the streamwise characteristics of the far-wake could be superimposed with the wake meandering process, which is a crosswise characteristic of the flow, and they can influence the downstream turbine within the array in terms of fatigue loadings. In the final part of this study, the influence of the imposed motions on the available power of the far-wake meandering is investigated. Available power in a disc with the diameter D of the porous disc model, centred at the instantaneous wake centre, is calculated based on the measured velocity contours. The velocity contour is converted into the normalised power per area (W/m^2) field contours with (6).

$$P = \frac{1}{2} u \cdot |u|^2 \quad (6)$$

The normalised power time-series is formed for all test cases at the distance of $8.125 D$ and with a sampling rate of 14.1 Hz , similar to the image acquisition rate for the data acquisition stage. This time history is then converted into the frequency domain using the Welch method with 128 segments and 50% overlap for the time-series with the length of $t = 992.8 \text{ s}$. The resultant PSD spectrums are plotted in Figure 13. As shown, the frequency of imposed motion is also distinguishable in power fluctuation, leaving an influence of the imposed motion in far-wake of normalised power. A closer inspection of Figure 13 shows that, compared to the fixed reference case (blue dash line), Pitch motions (yellow and green lines) reduced the energy of the power fluctuations within frequencies below

their motion frequency. This result is aligned with previous experiments in the literature, for example see [15].

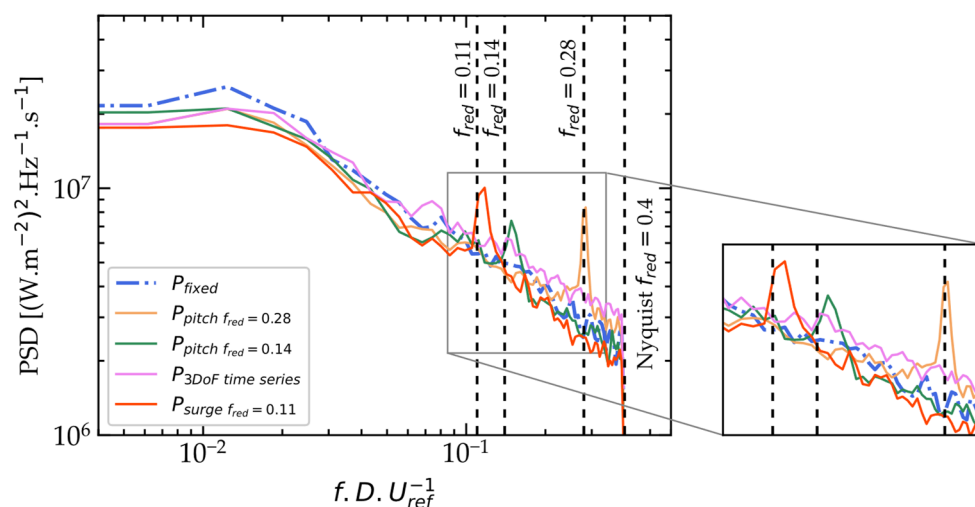


Figure 13. Power spectrum density (PSD) of porous disc wake power, measured at $x = 8.125 D$.

As discussed in [15], the Pitch motion induced a signature on the wake structure on the wind turbine model as well as its output power, which depends on the amplitude and frequency of the oscillations. Additionally, the current experimental study suggested that in terms of the wake meandering process, regardless of the amplitude and frequency, the frequency of the motion would exist in the PSD of available power in the turbines wake. Although the imposed motion does not show a strong effect on the cross-stream wake meandering, a great harmonic signature in the streamwise direction can be seen, which will travel through the wake of the rotor to the downstream turbine. This behaviour was also observed in surge motion by [17] on the streamwise velocity component. With reviewing the PSD of the power in Figure 13, the influence of the imposed motions on the average power shows a strong effect of weak motions, where a harmonic signature in the wake memory can be distinguished, although it does not look too intense. This harmonic signature exists in all the test cases regardless of the reduced frequency of the motions. Therefore, it shows that even for cases where motions frequency could not be observed in the lateral characteristics of the wake meandering process, this frequency still exists in the integrative metric of the wake in the streamwise direction, i.e., normalised power of the far-wake. It's like a pulsive wave travelling in the streamwise direction that can affect the second turbine downstream. The second turbine receives harmonic motions available in power from the upstream turbine, which can cause resonance in loadings.

4. Conclusions

This study investigated the influence of the imposed motions on the development of far-wake meandering of a floating wind turbine as a follow-up of [14]. A porous disc model is used for this study. The disc model experienced a typical neutral marine ABL, while the imposed surge, pitch, as well as 3DoF motion (Surge, heave, and Pitch) with multi-frequency time-series are applied to the model using a motion system. In order to conduct high-fidelity velocity field measurements, the S-PIV method is used at $8.125 D$ of the wind turbine model at a cross-section plan. The velocity contour is then post-processed to investigate the time-series of far-wake centres and normalised available power of far-wake in time and frequency domains.

There were three limitations associated with the current measurements. Firstly, having an acquisition rate of 14.1 Hz in the S-PIV measurements has resulted in a Nyquist frequency of 7.05 Hz, which limited the frequency domain investigations up to this folding frequency. Therefore, all designed test cases have motion frequency under this limit value. Secondly,

the results of the present experimental study are limited to only one type of prototype FOWT with a given sea state of the installed test site. Therefore, further investigation into different types of floating substructures and different turbines size in various sea states is required. Thirdly, using a porous disc to model the floating wind turbine instead of a rotating-blade model prevents the reproduction of all physical details in the near wake and the near-wake-moving rotor interactions. Since one deals here with the influence of length scales much larger than the rotor diameter, it can be expected that the draw conclusions are valid for a rotating wind turbine model. However, this last aspect needs to be checked.

This investigation found that imposed motions, including three DoF (Heave, surge, pitch) time-series with multi-frequency content, have no visible effect on the mean far-wake recovery. These results are in line with [14] which was focused only on surge motions. The velocity statistics, such as streamwise velocity, its standard deviation, and TKE have shown no sensitivity to imposed motions. This result was contradictory to [30] due to the different flow configurations used. Where in current research, the focus was mainly on the wake properties, while in [30] attention is made to turbine characteristics. Investigating how the wake dynamics translate into the performance of a downstream floating wind turbine remains to be done in the current research study.

The 2- and 1-dimensional histogram of the wake centre position is reviewed in the time domain for different test cases. The statistics of wake meandering, such as standard deviation, skewness, and kurtosis, have shown no significant statistical sensitivity to imposed motions. The study shows that the wake centres oscillation is clustered in the vertical direction and spread in the lateral direction regardless of imposed motions. Moreover, the lateral distribution of wake centres follows a Gaussian shape, while vertical distribution follows a skew-normal shape with negative skewness towards height increment. The PSD of different test cases have shown that the motion frequency could leave a peak in frequency spectrum, if the frequency motions was higher than limit value of reduced frequency equal to 0.15. This was a different case for the 3DoF motion; while lateral fluctuations were affected only after a reduced frequency of 0.15, the vertical oscillation had higher values of energy for all frequency ranges, leaving the conclusion that imposed motions might have a stronger influence on the vertical oscillation of far-wake centre while analysing 3DoF multi-frequency time series. While the monochromatic imposed motions with a reduced frequency of less than 0.15 do not strongly influence the cross-stream wake meandering, a significant harmonic signature (as a pulse wave) is still observable in the normalised power even for motion cases with a reduced frequency of less than 0.15.

This research has contributed to advancing the state-of-the-art in wave-structure-wind interactions for FOWTs. This is important since the frequency characteristics of the floater motion could act as a pulse wave and travel through the wake of the rotor to a downstream turbine and cause some resonance in the downstream turbine due to their induced pulsive loads. These facts suggest that it would be important for future research to examine and develop the far-wake dynamic models with consideration to the floating wind turbine motions on the wake meandering phenomena. Future research will address some of the limitations of the research presented in this paper, such as reconducting current test campaigns for different types of FOWT with different substructures, rotor model and capacity, and sea states. Additionally, reviewing the performance of a downstream wind turbine operating within the wake meandering of a moving upstream one remains to be done to confirm the recent results available in the literature.

Author Contributions: The current research article was a collaborative work among the authors. Conceptualization, methodology and data curation, N.B. and B.C.; writing—original draft preparation, software, formal analysis and visualisation, N.B.; validation, N.B., B.C., L.P. and S.A.; investigation, N.B., B.C., B.S. and L.P.; resources, S.A.; writing—review and editing, N.B., B.C., B.S., L.P., C.D., S.A.; supervision, B.C., J.M. and S.A.; project administration, S.A.; Funding acquisition FLOWER, C.D., J.M., S.A.; Funding acquisition WEAMEC, S.A., B.C., L.P. All authors have read and agreed to the published version of the manuscript.

Funding: This research is performed in the framework of the FLOWER project. This project has received funding from the European Union’s Horizon 2020 research and innovation programme under the Marie Skłodowska-Curie grant agreement N° 860879. This work is carried out within the framework of the WEAMEC, West Atlantic Marine Energy Community, and with funding from the Pays de la Loire Region.

Data Availability Statement: Data available upon request.

Acknowledgments: The test campaign is conducted in the atmospheric wind tunnel at the LHEEA Lab test facility at Ecole Centrale Nantes, France. All the efforts of engineers and technicians involved in preparing the lab for the experiment are highly acknowledged.

Conflicts of Interest: The authors declare no conflict of interest.

Nomenclature

Abbreviations		Symbols and Indices	
FOWT	Floating Offshore Wind Turbine	C_T	Thrust coefficient
WT	Wind Turbine	f	Frequency in Hz
S-PIV	Stereoscopic Particle Image Velocimetry	f_{red}	Reduced frequency
DoF	Degrees Of Freedom	U_{ref}	Reference velocity of incident wind in meter per second
3DoF	Three-degrees-of-freedom	U_{hub}	Reference velocity of wind at hub height in meter per second
ABL	Atmospheric Boundary Layer	H_s	Significant wave height in meter
BL	Boundary Layer	T_p	Wave peak period in second
2D3C	2-Dimensional-3-Component	Mpx	Megapixel
2D	2-Dimensional	px	Pixel
Nd-YAG	Neodymium-Doped Yttrium Aluminum Garnet	T_i	Turbulence intensity (%)
TKE	Turbulence Kinetic Energy	$\sigma_u, \sigma_v, \sigma_w$	Standard deviation of velocity component (x, y, z)
PDF	Probability Density Function	I_u	Streamwise Turbulence intensity (%)
PSD	Power Spectral Density	N_b	Number of independent samples
<i>Symbols and Indices</i>		$\epsilon_{(u)}$	Uncertainty of estimated streamwise mean-velocity
GW, MW, kW	Gigawatt, Megawatt, Kilowatt	ϵ_σ	Uncertainty of estimated standard deviation
D	Diameter of turbine rotor in meter	x, y, z	Space coordinates (streamwise, lateral and vertical, respectively)
α	Power-law exponent of ABL velocity profile	y_c, z_c	Instantaneous crosswise location of wake centre
a	Axial induction factor of porous disc	\bar{y}_c, \bar{z}_c	Mean crosswise location of wake centre
z_0	Roughness length of ABL in meter	$\Delta y, \Delta z$	Revised location of wake centre
L_u^x	Integral length scale of ABL in meter	$Y.D^{-1}$	Normalized lateral distance on rotor diameter
C_p	Power coefficient	z_{hub}	Hub height in meter

References

1. DNV GL. *Floating Wind: The Power To Commercialize*; DNV GL: Bærum, Norway, 2020.
2. El-Asha, S.; Zhan, L.; Iungo, G.V. Quantification of Power Losses Due to Wind Turbine Wake Interactions through SCADA, Meteorological and Wind LiDAR Data. *Wind Energy* **2017**, *20*, 1823–1839. [[CrossRef](#)]
3. Huang, Y.; Wan, D.; Hu, C. Numerical Study of Wake Interactions between Two Floating Offshore Wind Turbines. In Proceedings of the 28th International Ocean and Polar Engineering Conference, Sapporo, Japan, 10–15 June 2018; pp. 541–548.
4. Tang, H.; Lam, K.M.; Shum, K.M.; Li, Y. Wake Effect of a Horizontal Axis Wind Turbine on the Performance of a Downstream Turbine. *Energies* **2019**, *12*, 2395. [[CrossRef](#)]
5. Barthelmie, R.J.; Jensen, L.E. Evaluation of Wind Farm Efficiency and Wind Turbine Wakes at the Nysted Offshore Wind Farm. *Wind Energy* **2010**, *13*, 573–586. [[CrossRef](#)]
6. Sun, H.; Gao, X.; Yang, H. A Review of Full-Scale Wind-Field Measurements of the Wind-Turbine Wake Effect and a Measurement of the Wake-Interaction Effect. *Renew. Sustain. Energy Rev.* **2020**, *132*, 110042. [[CrossRef](#)]
7. Barthelmie, R.J.; Hansen, K.; Frandsen, S.T.; Rathmann, O.; Schepers, J.G.; Schlez, W.; Phillips, J.; Rados, K.; Zervos, A.; Politis, E.S.; et al. Modelling and Measuring Flow and Wind Turbine Wakes in Large Wind Farms Offshore. *Wind Energy* **2009**, *12*, 431–444. [[CrossRef](#)]
8. Meng, H.; Lien, F.S.; Glinka, G.; Li, L.; Zhang, J. Study on Wake-Induced Fatigue on Wind Turbine Blade Based on Elastic Actuator Line Model and Two-Dimensional Finite Element Model. *Wind Eng.* **2019**, *43*, 64–82. [[CrossRef](#)]
9. Urbán, A.M.; Liew, J.; Dellwik, E.; Larsen, G.C. The Effect of Wake Position and Yaw Misalignment on Power Loss in Wind Turbines. In *Journal of Physics: Conference Series*; IOP Publishing: Bristol, UK, 2019; Volume 1222.
10. Larsen, G.C.; Madsen, H.A.; Thomsen, K.; Larsen, T.J. Wake Meandering: A Pragmatic Approach. *Wind Energy* **2008**, *11*, 377–395. [[CrossRef](#)]
11. Yang, X.; Sotiropoulos, F. A Review on the Meandering of Wind Turbine Wakes. *Energies* **2019**, *12*, 4725. [[CrossRef](#)]
12. Porté-Agel, F.; Bastankhah, M.; Shamsoddin, S. *Wind-Turbine and Wind-Farm Flows: A Review*; Springer: Dordrecht, The Netherlands, 2020; Volume 174, ISBN 1054601900473.

13. Argyle, P.; Watson, S.; Montavon, C.; Jones, I.; Smith, M. Modelling Turbulence Intensity within a Large Offshore Wind Farm. *Wind Energy* **2018**, *21*, 1329–1343. [[CrossRef](#)]
14. Pardo Garcia, L.; Conan, B.; Aubrun, S.; Perret, L.; Piquet, T.; Raibaud, C.; Schliffke, B. Experimental Analysis of the Wake Meandering of a Floating Wind Turbine under Imposed Surge Motion. *J. Phys. Conf. Ser.* **2022**, *2265*, 042003. [[CrossRef](#)]
15. Fu, S.; Jin, Y.; Zheng, Y.; Chamorro, L.P. Wake and Power Fluctuations of a Model Wind Turbine Subjected to Pitch and Roll Oscillations. *Appl. Energy* **2019**, *253*, 113605. [[CrossRef](#)]
16. Kadum, H.; Rockel, S.; Hölling, M.; Peinke, J.; Cal, R.B. Wind Turbine Wake Intermittency Dependence on Turbulence Intensity and Pitch Motion. *J. Renew. Sustain. Energy* **2019**, *11*, 53302. [[CrossRef](#)]
17. Schliffke, B.; Aubrun, S.; Conan, B. Wind Tunnel Study of a “Floating” Wind Turbine’s Wake in an Atmospheric Boundary Layer with Imposed Characteristic Surge Motion. *J. Phys. Conf. Ser.* **2020**, *1618*, 062015. [[CrossRef](#)]
18. BW-ideol FLOATGEN 2MW Demonstration FOW System. Available online: <https://www.bw-ideol.com/en/academic-publications> (accessed on 1 January 2022).
19. Savory, E.; Perret, L.; Rivet, C. Modelling Considerations for Examining the Mean and Unsteady Flow in a Simple Urban-Type Street Canyon. *Meteorol. Atmos. Phys.* **2013**, *121*, 1–16. [[CrossRef](#)]
20. Raibaud, C.; Piquet, T.; Schliffke, B.; Conan, B.; Perret, L. POD Analysis of the Wake Dynamics of an Offshore Floating Wind Turbine Model. *J. Phys. Conf. Ser.* **2022**, *2265*, 022085. [[CrossRef](#)]
21. Schliffke, B. Experimental Characterisation of the Far Wake of a Modelled Floating Wind Turbine as a Function of Incoming Swell. Ph.D. Thesis, Ecole Centrale Nantes, Nantes, France, 2022.
22. VDI 2000 *Umweltmeteorologie*; Environmental Meteorology—Dispersion of Emissions by Accidental Releases. VDI: Berlin, Germany, 2019.
23. Ecole Centrale De Nantes SEM-REV Test Site. Available online: <https://sem-rev.ec-nantes.fr/> (accessed on 1 January 2022).
24. Aubrun, S.; España, G.; Loyer, S.; Hayden, P.; Hancock, P. *Is the Actuator Disc Concept Sufficient to Model the Far-Wake of a Wind Turbine?* Oberlack, M., Peinke, J., Talamelli, A., Castillo, L., Hölling, M., Eds.; Springer: Berlin/Heidelberg, Germany, 2012; pp. 227–230.
25. Kähler, C.J.; Astarita, T.; Vlachos, P.P.; Sakakibara, J.; Hain, R.; Discetti, S.; La Foy, R.; Cierpka, C. Main Results of the 4th International PIV Challenge. *Exp. Fluids* **2016**, *57*, 97. [[CrossRef](#)]
26. Benedict, L.H.; Gould, R.D. Towards Better Uncertainty Estimates for Turbulence Statistics. *Exp. Fluids* **1996**, *22*, 129–136. [[CrossRef](#)]
27. Sciacchitano, A. Uncertainty Quantification in Particle Image Velocimetry. *Meas. Sci. Technol.* **2019**, *30*, 092001. [[CrossRef](#)]
28. Nobach, H.; Tropea, C. *Fundamentals of Data Processing BT—Springer Handbook of Experimental Fluid Mechanics*; Tropea, C., Yarin, A.L., Foss, J.F., Eds.; Springer: Berlin/Heidelberg, Germany, 2007; pp. 1399–1417. ISBN 978-3-540-30299-5.
29. Chamorro, L.P.; Porté-Agel, F. A Wind-Tunnel Investigation of Wind-Turbine Wakes: Boundary-Layer Turbulence Effects. *Bound.-Layer Meteorol.* **2009**, *132*, 129–149. [[CrossRef](#)]
30. Ramos-García, N.; Kontos, S.; Pegalajar-Jurado, A.; González Horcas, S.; Bredmose, H. Investigation of the Floating IEA Wind 15 MW RWT Using Vortex Methods Part I: Flow Regimes and Wake Recovery. *Wind Energy* **2022**, *25*, 468–504. [[CrossRef](#)]
31. Ramos-García, N.; González Horcas, S.; Pegalajar-Jurado, A.; Kontos, S.; Bredmose, H. Investigation of the Floating IEA Wind 15-MW RWT Using Vortex Methods Part II: Wake Impact on Downstream Turbines under Turbulent Inflow. *Wind Energy* **2022**, *25*, 1434–1463. [[CrossRef](#)]
32. Taylor, G.J.; Milborrow, D.J.; McIntosh, D.N.; Swift-Hook, D.T. Wake Measurements on the Nibe Windmills. In Proceedings of the 7th British Wind Energy Association Conference, Oxford, UK, 27–29 March 1985.
33. Coudou, N.; Moens, M.; Marichal, Y.; Van Beeck, J.; Bricteux, L.; Chatelain, P. Development of Wake Meandering Detection Algorithms and Their Application to Large Eddy Simulations of an Isolated Wind Turbine and a Wind Farm. *J. Phys. Conf. Ser.* **2018**, *1037*, 72024. [[CrossRef](#)]